Insights into controlling bacterial cellulose nanofiber film properties through balancing thermodynamic interactions and colloidal dynamics

Journal:	*Molecular Systems Design & Engineering*
Manuscript ID	ME-ART-03-2024-000058.R1
Article Type:	Paper
Date Submitted by the Author:	11-May-2024

Complete List of Authors:	Mandal, Aban; University of Washington, Materials Science and Engineering Liao, Kuotian; University of Washington, Materials Science and Engineering Iyer, Hareesh; University of Washington, Materials Science and Engineering Lin, Junhao; University of Washington, Materials Science and Engineering Li, Xinqi; University of Washington, Materials Science and Engineering Zhang, Shuai; University of Washington, Materials Sciences and Engineering; Pacific Northwest National Laboratory, Roumeli, Eleftheria; ETH Zürich

MATERIALS SCIENCE & ENGINEERING
UNIVERSITY of WASHINGTON

Eleftheria Roumeli
Assistant Professor
337 Roberts Hall, Box 352120
Seattle, WA 98195-2120
Email: eroumeli@uw.edu
Tel.:+1 206-616-2832

'Design, System, Application' statement.

Our study presents a molecular design strategy to optimize the mechanical properties of bacterial cellulose nanofiber (CNF) films by precisely controlling thermodynamic and electrokinetic interactions within colloidal dispersions. By manipulating the Hansen solubility parameters, we fine-tuned CNF-solvent molecular interactions, thus governing the CNFs' assembly from a colloidal to a solid state. The resulting fibrillar arrangements were directly correlated with the mechanical properties of the films, yielding strengths ranging from 20-150 MPa and Young's moduli from 1-10 GPa. Our approach emphasizes the interplay between solvent characteristics, dispersion behavior, and subsequent film formation, providing a robust framework for advancing CNF processing techniques. The system functionality focused on optimizing colloidal stability and assembling behavior transition thresholds in varied solvent environments, enhancing the quality of CNF films. Immediate applications of our work lie in developing environmentally sustainable materials (fully biobased) with mechanical properties tailored for specific uses, advancing the broader adoption of nanocellulose in engineering applications. Our insights pave the way for future material innovations, where the precision in colloidal processing equips engineers with the capability to predict and control the macroscopic properties of CNF-based composites.

Journal Name

ARTICLE TYPE

Cite this: DOI: 00.0000/xxxxxxxxxx

Insights into controlling bacterial cellulose nanofiber film properties through balancing thermodynamic interactions and colloidal dynamics

Aban Mandal [a], Kuotian Liao [a], Hareesh Iyer [a], Junhao Lin[a], Xinqi Li[a], Shuai Zhang[a,b,c], and Eleftheria Roumeli[a*]

Received Date
Accepted Date

DOI: 00.0000/xxxxxxxxxx

In recent years, nanocellulose has emerged as a sustainable and environmentally friendly alternative to traditional petroleum-derived structural polymers. Sourced either from plants, algae, or bacteria, nanocellulose can be processed into colloid, gel, film and fiber forms. However, the required fundamental understanding of process parameters that govern the morphology and structure-property relationships of nanocellulose systems, from colloidal suspensions to bulk materials, has not been developed and generalized for all forms of cellulose. This further hinders the more widespread adoption of this biopolymer in applications. Our study investigates the dispersion of cellulose nanofibers (CNFs) produced by a bacterial-yeast co-culture, in solvents, highlighting the role of thermodynamic interactions in influencing their colloidal behavior. By adjusting Hansen solubility parameters, we controlled the thermodynamic relationship between CNFs and solvents across various concentrations, studying the dilute to semi-dilute regimes. Rheological measurements revealed that the threshold at which a concentration-based regime transition occurs is distinctly solvent-dependent. Complementing rheological analysis with small angle X-ray scattering and zeta potential measurements, our findings reveal that enhancing CNF-solvent interactions increases excluded volume in the dilute regime, emphasizing the importance of the balance between fiber-fiber and fiber-solvent interactions. Moreover, we investigated the transition from colloidal to solid state by creating films from dispersions with varying interaction parameters in semi-dilute regimes. Through mechanical testing and scanning electron microscopy imaging of the fracture surfaces, we highlight the significance of electrokinetic effects in such transitions, as dispersions with higher electrokinetic stabilization gave rise to stronger and tougher films despite having less favorable thermodynamic interaction parameters. Our work provides insights into the thermodynamic and electrokinetic interplay that governs bacterial CNF dispersion, offering a foundation for future application and a deeper understanding of nanocellulose's colloidal and structure-property relationships.

1 Introduction

Nanocellulose in its various forms, including nanofibers (CNF) and nanocrystals (CNC) derived from plants as well as bacterial sources[1,2], has been widely studied with a significant body of literature focusing on understanding the remarkable mechanical properties of the various nanocellulose forms and their applications[3–6]. Typically, following the initial steps of extraction from plants or purification from bacteria cultures, a defibrillation process gives rise to nanocellulose which is suspended in a solvent before being further processed and/or mixed with other materials. Therefore, the stability of colloidal suspensions of nanocellulose is a key element in the processing route, as it directly influences the state of aggregation that will be present for the subsequent processing steps. Colloidal stability depends on the solute-solvent, solute-solute, and solvent-solvent interactions, which have been studied in the past for nanocellulose colloids[7]. While nanocellulose dispersions have been predominantly studied in aqueous media because of their affinity to water[8], it is important to un-

[a] Department of Materials Science and Engineering, University of Washington, Seattle WA 98195, USA. E-mail: eroumeli@uw.edu
[b] Molecular Engineering & Sciences Institute, University of Washington, Seattle, WA 98195, USA.
[c] Physical Sciences Division, Pacific Northwest National Laboratory, Richland, WA99354, USA.

† Electronic Supplementary Information (ESI) available: [details of any supplementary information available should be included here]. See DOI: 00.0000/00000000.

derstand the stability of a colloidal dispersion across various media so that a better dispersed and more stable colloidal system can be developed. Studies previously undertaken specifically for nanocellulose, emphasized the role of cohesive energy, surface energy, and thermodynamic parameters to understand the dispersibility of cellulose[7,9].

Solubility parameters play an important role in the dispersion stability and solvent systems can be developed, such that the polar, dispersive, and hydrogen bonding cohesive energies of the solvent complement that of nanocellulose[10]. To understand these nanocellulose-solvent interactions, previous research has highlighted the variations in solubility parameters among different types of nanocellulose, specifically CNCs and CNFs[11]. There is a slight difference of 0.6 $MPa^{1/2}$ in the dispersive solubility parameter, with CNCs having 17.40 $MPa^{1/2}$ and CNFs having 16.8 $MPa^{1/2}$. Conversely, the polar solubility parameter shows almost no difference, with values of 10.5 $MPa^{1/2}$ for CNCs and 10.4 $MPa^{1/2}$ for CNFs. The difference in the hydrogen bonding solubility parameter is more significant, at 1.5 $MPa^{1/2}$, with CNCs at 18.1 $MPa^{1/2}$ and CNFs at 16.6 $MPa^{1/2}$ [11]. Such subtle variations in solubility parameters can be attributed to the differences in surface chemistry and crystallinity between these types of nanocellulose. While extensive research has confirmed the applicability of qualitative models based on Hansen Solubility parameters for nanocellulose colloidal stability[7,9,12], yet, the effect of thermodynamic interactions between solvent and nanocellulose on colloidal properties remains largely unexplored. Further, there is a need to account for the synergy between thermodynamic and electrokinetic interactions for a better understanding of the colloidal behavior of nanocellulose when using solubility parameter-based models, and more importantly for connecting those findings to properties of bulk cellulose materials produced from the colloidal state.

In order to control colloidal stability and enable subsequent processing into bulk materials or composites, surface modifications, either physical through defibrillation or chemical though functionalization, have been extensively studied[13,14]. Wägberg et al. demonstrated that the surface modification of CNF through the substitution of hydroxyl groups with carboxymethyl group gives rise to well-dispersed fibers in aqueous media, such that agglomeration was prevented by the deprotonation of the carboxymethyl group, driven by electrostatic repulsion[15]. Such surface charge formation can be achieved by controlling the pH and ionic concentration of the selected solvent[16]. Molnes et al. reported that the stability of CNC dispersions improves when sulfate groups are introduced following esterification of the surface hydroxyl groups of cellulose during the hydrolysis processing of CNCs[17]. Further works on the effects of the choice of acid media for hydrolysis on the dispersion stability showed that HCl hydrolyzed CNCs had inferior stability than the H_3PO_4 and H_2SO_4 hydrolyzed ones, however the latter lacked thermal stability[18–20]. The improved colloidal stability was attributed to the reduction of hydrogen bonding in the hydroxyl groups[21]. Such reduction can also be achieved using inorganic ions, surfactants, and changing the chemical environment along with the hydrolysis process[22–27]. To provide insights into CNF interactions with cationic polyelectrolytes, Wägberg et al.[16] created a model based upon the DLVO theory[28,29], which asserted that the pH has a stronger influence than ionic interaction and predicted a surface charge development of 90 mC/m^2 for CNF at pH 7. Such high charge density implies counterion condensation[30] along with specific counter ion and surface charge interaction[31]. This model was extended by Fall et al.[32] to include these interactions and further correlated semi-quantitatively salt concentration and pH with colloidal stability. Other methods such as mechanical blending, use of shear through micro fluidization[33] and ultrasonication have been extensively reported for the preparation of CNF and showed lower electrokinetic potential than their counterparts prepared using chemical routes.

In this work, we focus on understanding the effects of thermodynamic CNF-solvent interactions on the colloidal behavior of the dispersions, and the electrokinetic interactions that explain the deviations from the predicted behavior. We further highlight the connections between the synergy of electrokinetic and thermodynamic interactions in the colloidal state to the mechanical properties of cellulose nanofiber films obtained in the solid state.

2 Materials and Methods

2.1 Experimental Methods

2.1.1 Growth of Bacterial Cellulose

Bacterial cellulose was produced as previously described by Balistreri et al.[34]. Briefly, we inoculated blended commercially available kombucha starter (SCOBY) in 4 liters of media (tea and 800 g of sugar). After, inoculation, the culture was incubated at room temperature (25 °C) in a glass container under static conditions for 14 days. The pellicle consisting of bacterially synthesized cellulose nanofibers formed at the air/liquid interface was harvested and purified under alkaline conditions by soaking in 1 M NaOH for 24 hours, followed by immersing in deionized water (DI) to remove the impurities until the pellicle became white and exhibited a neutral pH. The cleaned bacterial cellulose pellicles were washed using hot water (90 - 100°C) followed by mechanical disintegration for 10 minutes using a blender (Ninja BL770 Mega Kitchen System, 1500W) without adding any excess water. The aqueous disintegrated cellulose suspensions will be referred to hereinafter as CNF suspensions.

2.1.2 Preparation of CNF Colloids

To prepare dispersions with the desired CNF concentration, we diluted a 1 wt.% dispersion using the desired solvents. For water suspensions, we added DI and prepared dispersions of 0.031, 0.066, 0.125, 0.2, and 0.325 wt.% For the water/IPA solvent mixtures, we prepared dispersions of 0.075, 0.05, 0.03, 0.02,0.01, 0.0075, 0.005, 0.002 and 0.001 wt.% The concentrations of all the prepared dispersions were validated by using a moisture analyzer (VWR 53M.H). All moisture analysis experiments were conducted in triplicates.

2.1.3 Preparation of CNF Films

220g of 0.2 wt% CNF dispersions in the different solvents were vacuum-filtered using a membrane filter with a pore diameter of $8\mu m$ (Whatman Grade 2 Filter Paper, 150mm dia) for 2 hours to form a stiff gel film. The formed gel film was then removed from

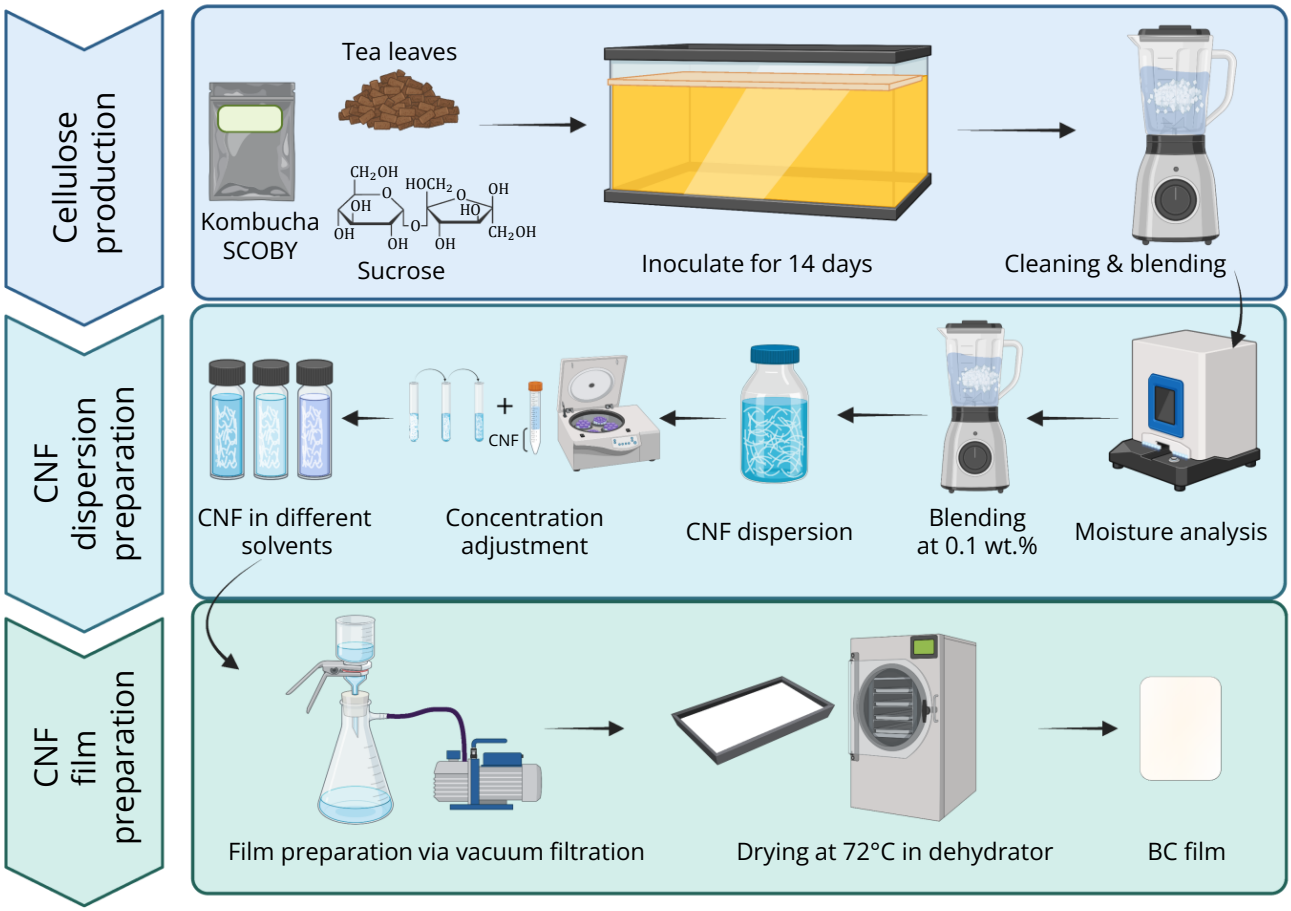

Fig. 1 Experimental methodology. Bacterial cellulose growth, preparation of CNF dispersions and films. Created with Biorender.com.

the vacuum filtration apparatus, peeled carefully, and transferred between two glass plates to prevent curling during the final dehydration process. The final solvent was removed by evaporation at 78°C in a dehydrator. Once the solvent was completely removed, the film was placed in a vacuum desiccator before testing.

2.2 Characterization Methods

2.2.1 Scanning Electron microscopy

To image the CNFs, we drop cast 50μL of 0.03 wt.% CNF dispersion on a silicon wafer using a pipette and let the drop dry under a vacuum desiccator. For imaging the CNF films, we first coated them with 4nm platinum using an EM ACE600 sputter coater (Leica Microsystems GmbH; Wetzlar, Germany) and then imaged them on an Apreo VP SEM (Thermo Fisher Scientific; Waltham, MA, USA), operating at an accelerating voltage of 2 kV and a current of 10 pA.

2.3 Atomic Force Microscopy

Particles were subjected to ultrasonication using a Fisher Scientific Model 505 probe sonicator (Thermo Fisher, Waltham, MA, USA) and then diluted to approximately 0.0001 wt.% DI. Subsequently, 50 μL of the resulting sample suspension was cast onto a freshly cleaved mica substrate (Ted Pella, Redding, CA) and allowed to dry in ambient conditions. Imaging of the samples was performed using tapping mode on a Dimension Icon AFM (Bruker Corporation, Billerica, MA), employing a Multi75−G AFM probe (Budget Sensors, Sofia, Bulgaria) with a force constant of 3.0 N m^{-1} and a resonance frequency of 75 kHz. Offline data processing was carried out using NanoScope Analysis software (Bruker Corporation, Billerica, MA). To measure fiber thickness, both single fibers and fiber bundles were analyzed separately. Each fiber was sampled three times, with a total of 27 to 70 measurements taken from 3 to 5 technical replicates. Additionally, for each fiber, measurements were collected individually (n=20-70).

2.3.1 Surface Charge Density Measurements

100g of 0.05 wt% CNF dispersion in 0.2 mM HCl solution and 10 mM NaCl solution was titrated by 0.1 mM NaOH solution while simultaneously taking pH (VWR sympHony B10P) and conductivity (Oakton Cond 6+) measurements in triplicates. The concentrations of the HCl, NaOH, and NaCl are taken such that the ionic strength of the resulting solution always remains constant.

2.3.2 Zeta Potential

The zeta potential was measured by Dynamic Light Scattering using a Malvern Zetasizer Nano ZS (Malvern Panalytical, Worcester-

shire, UK). CNF dispersions with a concentration of 0.005 wt.% were prepared across a pH range of 3 to 10 by adjusting with 20 mM solutions of HCl and NaOH. To ensure constant ionic activity across all samples measured for zeta Potential, a consistent NaCl concentration of 5 mM was maintained. The zeta potential samples for CNF dispersions in different solvents were prepared similarly, such that a NaCl concentration of 5 mM was maintained but without the addition of any acid or base.

2.3.3 Rheological Studies

All rheological tests were conducted using an Anton Paar MCR 301 Rheometer either in a 25mm parallel plate setup with a plate gap of 0.5 mm (tests of 0.031, 0.066, 0.125, 0.2 and 0.325 wt.% CNF dispersions in water), or using a double gap system (tests of 0.1, 0.075, 0.05, 0.03, 0.02,0.01, 0.0075, 0.005, 0.002, and 0.001 wt.% CNF dispersions in water and water/IPA solvents). All experiments were carried out at a temperature of 25°C unless mentioned otherwise. The viscous response was measured under a controlled shear rate, in the range of 0.01 s^{-1} to 100 s^{-1} with a measurement time of 15s and with measurement points varying linearly with the shear rate. The viscous response was measured in 3 intervals as the shear rate was ramped from 0.01 s^{-1} to 1 s^{-1}, then from 1 s^{-1} to 0.01 $s^{-1}$and again from 0.01 s^{-1} to 1 s^{-1}. For identifying the linear viscoelastic regime, an amplitude sweep from 0.5 % to 100% at a frequency of 1 Hz was run with a measurement time of 25 s and with measurement points varying with a slope of 7 pts/decade. Finally, the frequency sweep was run at an amplitude of 5% from an angular frequency of 0.05 rad/s to 500 rad/s, with no time setting for measurement time and with measurement points varying with a slope of 5 pts/decade. For the tests conducted using the double gap system, the frequency sweep was run at an amplitude of 1% from an angular frequency of 0.05 rad/s to 100 rad/s and the viscous response was measured under a controlled shear rate, in the range of 10 s^{-1} to 1000 s^{-1} with a measurement time of 60s to 5s varying in logarithmic manner.

The data was fitted with the Carreau model given by:

$$\eta_{\text{carreau}} = \eta_\infty + (\eta_0 - \eta_\infty)\left(1 + \lambda\dot{\gamma}^2\right)^{\frac{n-1}{2}} \quad (1)$$

where, η_∞ is the infinite shear viscosity,η_0 is the zero shear viscosity, n is the shear thinning index and λ is the longest relaxation time.

The zero shear specific viscosity was calculated using the zero shear viscosity from the Carreau fit as,

$$\eta_{sp,0} = \eta_{rel} - 1 = \frac{\eta_0}{\eta_{solvent}} - 1 \quad (2)$$

where, $\eta_{solvent}$ is the viscosity of the solvent and η_{rel} is the relative viscosity.

The mobility constraints imposed in the volume-arrested states in polymer colloids were quantitatively studied through the Crowding Factor N, which correlates the number of rods/fibrils that occupy a spherical volume with a diameter equal to the length of the rod/fibril and is given by:

$$N_{3D} = \frac{2}{3}\phi a^2 \quad (3)$$

where ϕ is the volume fraction and a is the aspect ratio of the nanocellulose.

2.3.4 X-ray Scattering

Small-angle X-ray Scattering (SAXS) and Extra Small Angle X-ray scattering (ESAXS) data of CNF dispersions in different solvents were collected using a Xenocs Xeuss 3.0 with a wavelength of 1.54 A^{-1} from a CuK_α source. Samples were loaded in flow-through quartz capillaries (1 mm outer diameter) in a capillary stage. SAXS were collected for a 300 and ESAXS for 600 s, covering the q range from 0.002 to 0.1 A^{-1}. CNF suspensions in the three different solvents at the concentration of 0.001 wt.% were studied. For background subtraction, the capillaries containing the solvents and empty sample capillaries were also measured. The procedures of merging, background subtraction, and 1D SAXS Guinier fitting as well as BIFT Fitting were performed using BioXTAS Raw Software[35].

2.3.5 Mechanical testing

The films were cut in stripes of 60 mm by 4 mm and the thickness of each sample was measured in triplicates. Tensile testing was carried out on an Instron 5585H test frame with a 50N load cell. The distance between grips was 40 mm, and the nominal gauge length (on which extension and strain were measured and calculated) was 25mm. Extension of the gauge region was tracked during testing using an Instron Advanced Video Extensometer (2663-821), from which engineering strain was calculated. The rate of displacement was 0.2mm/sec.

3 Results and Discussion

In Figure 2, photographs of the colloidal state of CNFs in water at pH 6.5 are provided along with a characteristic SEM and AFM images and the corresponding fiber size analyses. The CNF colloids at concentrations ranging from 0.001 wt.% to 0.1 wt.% at pH 6.5 are depicted at time 0 and after 48h (Figure 2a), revealing their aggregation and flocculation behavior. The dispersions above the concentration of 0.03 wt.% show restricted fiber mobility and less flocculation, owing to the formation of a stable network.The 0.02 wt% sample shows a different phase inversion behavior, due to the presence of air bubbles in the flocculated network. In the absence of air bubbles in the 0.02 wt% sample shows similar behavior as the rest (SI Figure S12). The SEM image of 0.03 wt.% sample (Figure 2b) shows cellulose nanofibers with an average fiber diameter of 40 $\pm$ 14.79 nm. AFM images of sonicated 0.0001 wt.% samples (Figure 2d) reveal the characteristic cellulose hierarchical assembly where elemental fibrils with a diameter of 7.8 $\pm$ 2.89 nm are right-hand twisted into larger fibers with an average fiber diameter of 26.5 nm $\pm$ 7.42, in agreement with prior literature for bacterial cellulose fibers[36]. The AFM images also highlight kinks and bends in the CNFs in addition to a high degree of entanglement, which are characteristic of CNFs from bacterial cellulose. Overall the microscopy images demonstrate the hierarchical nature of CNFs, ranging from individual cellulose chains assembling into nanofibrils (also referred to as fibrils), which further assemble into nanofibers (held together primarily by interfibrillar hydrogen bonding), and even-

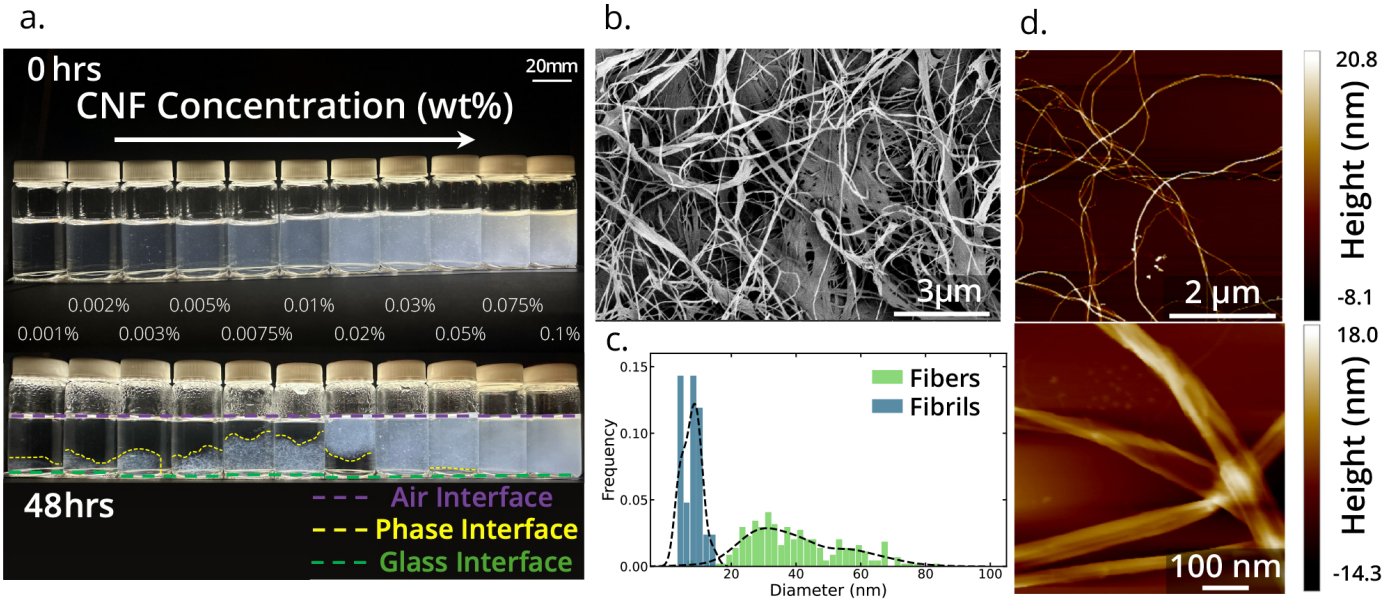

Fig. 2 CNF suspension stability and fiber morphology. (a) Timescale images of CNF dispersions at t=0 and t=48 h with concentrations ranging from 0.001 to 0.1 wt.% in water at a pH of 6.5. (b) SEM image of 0.03 wt.% dispersion. (c) Fiber diameter analysis from SEM (n>200) and fibril diameter analysis from AFM (n=20). (d) AFM images of 0.0001 wt.% dispersion

tually, these nanofibers form larger microfibers (held together by Van der Waal's forces).

3.1 Zeta Potential and Surface Charge Measurements

The zeta potential measurements of CNF dispersions (Figure 3) shed light on the electrokinetic behavior of these nanofibers in aqueous environments. The zeta potential at pH 7 was measured to be -14.91 $\pm$ 0.55 mV, indicating the formation of negative surface charges in water. This value is consistent with prior literature for unmodified CNFs where the surface hydroxyl functional groups contribute to the zeta potential[34,37]. As the pH becomes acidic the absolute zeta potential reduces and under highly acidic conditions (pH of 3.5) a minimum value of -4.07 $\pm$ 0.21 mV is observed. Such suppression can be attributed to the protonation of surface charges by the H^+ ions. As the pH becomes basic, the absolute zeta potential value increases. At a pH of 9, the maximum value of -16.9 $\pm$ 1.6 mV is observed. Upon further pH increase to 10, the absolute zeta potential decreases to -11.18 $\pm$ 0.81 mV. This behavior is consistent with prior reports on the electrokinetic behavior of CNFs and can be explained by Manning's counter-ion condensation[38]. That is, as the counter ion concentration increases due to an increase in Na^+ ion concentration on the addition of NaOH, beyond a concentration there is a suppression in the zeta potential. The measured zeta potential values signify that the colloidal CNF particles are not stable, as, generally, stable dispersions are considered to have an absolute zeta potential value $>$ 30 mV. This lack of "native" electrostatic stabilization is due to the absence of functional groups, besides the abundant hydroxyl groups, that can dissociate generating high surface charges.

The surface charge density estimation (SI Figure S1) further supports the zeta potential measurements. The CNF in this study was measured to have a surface charge density of 5.63 mmol e Kg^{-1} or 0.00563 mmol e g^{-1}. Such low surface charge densities are consistent with literature where CNFs from HCl hydrolyzed bacterial cellulose (without any surface functionalization) were reported to have surface charge densities of the same order of magnitude[39]. Thus, our results indicate that CNFs from bacterial cellulose without any further surface modification have low surface charge density, resulting in low electrostatic potential. The minimal electrokinetic contribution makes CNFs prone to aggregation, supporting our macroscopic observations of flocculation for concentrations below 0.2 wt.%.

3.2 Rheology

Rheological tests are reported in Figure 3c-e. First, looking at the viscous response of CNF dispersions versus shear rates, we distinguish four shear rate-based Regions, which are consistent with prior CNFs reports[40]. Between the shear rate range of $0.01s^{-1}$ to 0.03 s^{-1}, a low shear rate Newtonian Plateau is observed for fiber concentrations below 0.2 wt.% (marked as Region I in Figure 3d). In that range, the shear rate is sufficiently low so that the fibers cannot overcome their entanglement as strain is induced on them. Beyond a certain critical threshold shear rate given by$\lambda^{-1}1$, the fibers start aligning in the shear direction due to a shear-induced rotation of the fibers. This behavior is marked by a shear-thinning region (Region II in Figure 3d) seen for all concentrations in the range between λ^{-1} to 10 s^{-1}. For higher shear rates ($\dot{\gamma}$ >50), a high-shear Newtonian Plateau is observed (Region III in Figure 3e). However, we note that the high-shear Newtonian plateau is not consistently observed for all concentrations. In fact, we observed a larger deviation from the plateau in the cases of 0.125 and 0.2 wt.%. Instead, for these concentrations we measured a viscosity increase. We propose that this is due to hydro cluster formation which leads to a slight increase in viscosity, at the

studied range of shear rates (visually observed in the rheometer sample photos and schematically represented in Figure 3b). Hydro clusters here refer to the clusters of cellulose nanofibers that form in the shear direction due to flow-induced hydrodynamic interactions within the fluid (as can be seen in the graphical representation in Figure 3b). The formation of hydro clusters affect the rheological properties, such as viscosity and storage modulus in a colloid, particularly when the colloid is subjected to shear stresses. A shear thinning behavior is observed again upon further increase of the shear rate (Region IV in Figure 3e), where the hydro clusters/fiber domains align in the shear direction.

From prior literature, we know that at low CNF concentrations fiber entanglements prevent the formation of many hydro clusters[41]. Above a gel crowding factor (theoretically estimated to be $(N_{3D} = 16)$[41,42] an interconnected flocculated system is formed and above the rigidity threshold (theoretically estimated to be $N_{3D} = 60$) a coherent fiber floc with mechanical network strength is established. Our viscosity data comply with those observations as they collectively suggest four distinct concentration-defined regimes in the CNF suspensions. At low concentrations, the entangled fiber network is weak and can be aligned in the shear direction, while for higher concentrations hydro cluster formation resists the flow. As shown in the sample images in Figure 3b, beyond a certain threshold concentration ($\approx$ 0.2 wt.%), CNFs form a large cluster or floc which phase separates from the solvent at higher shear rates[42–44].

To enrich our understanding of the viscous response of our colloids, we apply the Carreau Model (See Methods and equation 1) in the viscosity data (Figure4a and fitting parameters summarized in Table 1). The data is fitted from 0.01 s^{-1} to 1 s^{-1} to capture the first 3 regions accurately since the Carreau model does not take into account the formation of hydro clusters which is observed beyond the shear rate of 1 s^{-1}. Specific zero shear viscosity ($\eta_{sp,\circ}/\eta_{water} - 1$) was plotted against volume fraction (Figure 4b) and fitted with a power law equation, $\eta_{sp,\circ} = a\phi^b$, where a is the constant coefficient and b is the scaling exponent and describes the concentration regimes. The $\eta_{sp,\circ}$ first scaled $\approx \phi^{1.345}$ and then $\approx \phi^{4.134}$ both these scaling exponents are in agreement with the theoretically estimated scaling exponent of 1.3-2 for semi-dilute regime and 4.67 for entangled regimes, for athermal dispersions[42,45,46]. The concentration threshold ϕ_e that separates the semi-dilute and entangled regimes represents the entanglement volume fraction. In concentrations above that threshold, CNFs start getting entangled with 3 contacts per fiber, which based on literature corresponds to a crowding factor N_{3D}= 60.[41,42] The onset of entanglement was calculated to be at a volume fraction of $\phi_e = 7.034 \times 10^{-4}$ which roughly corresponds to 0.11 wt.% considering the density of cellulose to be 1.5 g/cm^3. The loss and storage moduli are found to increase with a higher slope against concentration beyond this entanglement threshold concentration (Figure 4c), which signifies higher network strength owing to the entanglement of fibers beyond the threshold concentration[47]. Given the crowding factor theoretical value of 60, and the entanglement volume fraction from our data, we can estimate the aspect ratio of the nanocellulose from equation 3 to be 358. While this does not take into account the correction required for polydispersity[48], this method serves as a rough estimation for aspect ratio which otherwise is indeed difficult to estimate for longer CNFs like those obtained from bacterial cultures.

C (wt.%)	$\eta_\circ$ (Pa.s)	η_{inf} (Pa.s)	λ (s)	n	R^2
0.031	5.12	0.244	25.31	-0.57	0.99
0.066	14.16	0.30	28.71	-0.77	0.99
0.125	72.08	0.35	55.66	-0.47	0.99
0.2	370.35	0.28	130.99	-0.23	1.0
0.325	2799.65	1.09	413.35	-0.13	0.99

Table 1 Carreau Fitting Parameters. Concentration (C), zero and infinite shear viscosities ($\eta_\circ, \eta_{inf}$), longest relaxation time (λ), shear thinning index (n), and fitting quality parameter (R^2).

3.3 Effect of Thermodynamic Parameter on Colloidal Properties

To study the effects of solvent-CNF interactions, we selected three solvents based on combinations of water and IPA. The three solvents used in this study are based on the Hansen solubility parameters, such that the interaction parameter χ can be minimized. The χ parameter is related to the solubility parameters through the following equation:

$$\chi = \frac{v}{kT}[(\delta_{D,A} - \delta_{D,B})^2 + (\delta_{P,A} - \delta_{P,B})^2 + (\delta_{H,A} - \delta_{H,B})^2] \qquad (4)$$

where v is the lattice volume, k is the Boltzman constant, T is the temperature, δ_D,δ_P,δ_H are the dispersive, polar and hydrogen bonding interaction parameters of the components A and B. The three solvents we chose are (i) 100% water (100% DI), (ii) 50% water / 50% IPA (50% DI) and (iii) 7.5% water / 92.5% IPA (7.5% DI), all given in v/v. To enable a semi-quantitative analysis of the thermodynamic interaction effects, we normalized the corresponding χ parameters by the interaction parameter of water and cellulose, thus resulting in cellulose-solvent interaction parameters being 1, 0.15 and 0.5 times that of the water-cellulose interaction parameter, respectively for each solvent (SI Figure S2). The viscosity of IPA-Water mixtures was obtained from previous literature to be 3.0 mPa.s for the 50% DI, and 2.15 mPa.s for 7.5% DI[49]. Similarly, the dielectric constants were found to be 20.95 and 43.68 for 50% DI and 7.5% DI[49]. In the case of IPA-containing solvents, we are technically limited in the minimum shear rates we can experimentally apply and measure reliable viscosities with a rotational rheometer. In cellulose colloid literature, shear rates of 100 s^{-1} have been largely used to address this challenge[42]. Our data (SI Figure S3) reveal a considerable shear thinning occurring in volume fractions that lie in the semi-dilute regimes for shear rates of 316 s^{-1}. Thus, the viscosity at 316 s^{-1} served as a proxy for the specific zero shear viscosity in the study we describe hereinafter. With that assumption, we plotted the specific viscosity at 316 s^{-1} versus the volume fraction for all three solvents in Figure 5 so that we can identify the distinct regimes. In the studied solvents, three distinct regions based on slope changes on the log-log scale can be identified. The scaling exponent for Region I and Region II was 0.79 and 1.35 for 50%

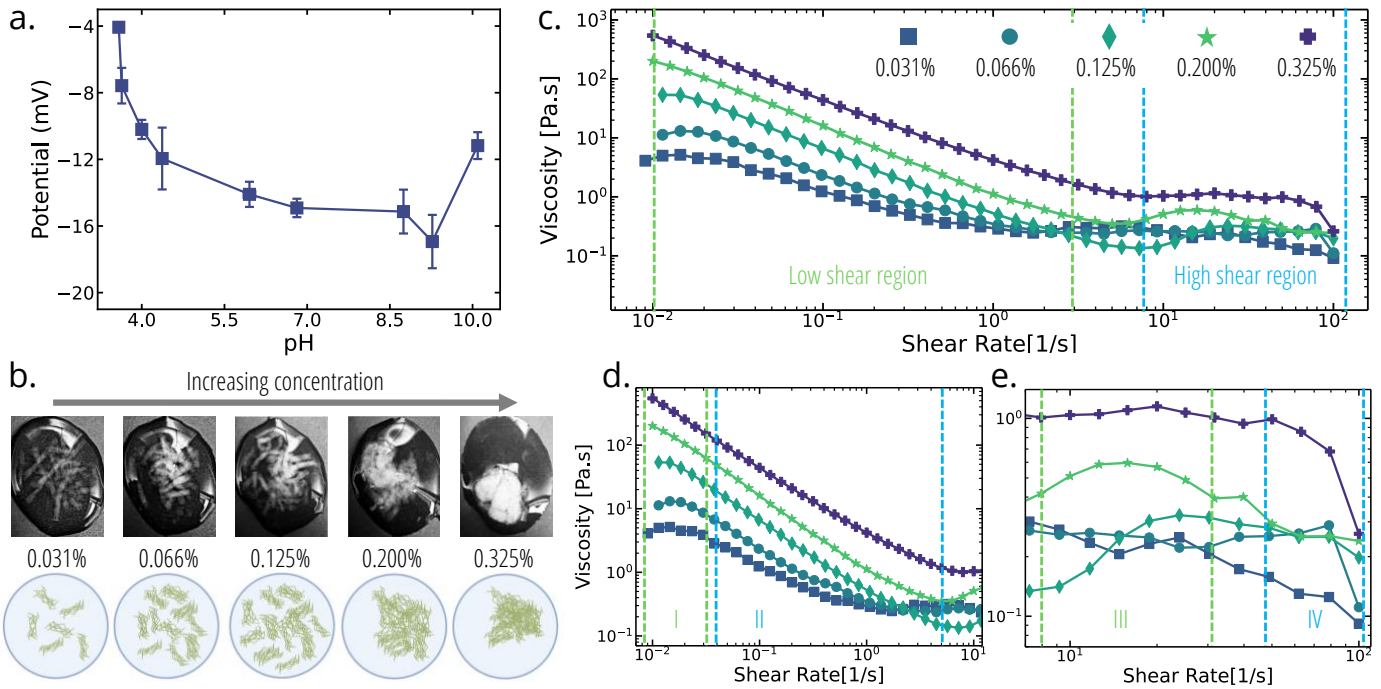

Fig. 3 Viscous Response of CNF Dispersions. (a) Zeta potential of CNF in water across pH of 2-10. (b) Optical images of CNF agglomerates/hydroclustes after application of high shear. (c) Viscosity versus shear rate in the complete shear rate range from $10^{-2}s^{-1}$ to $10^{2}s^{-1}$. (d) Viscosity versus shear rate in low shear regime($10^{-2}s^{-1}$ to $10^{1}s^{-1}$). (e) Viscosity versus shear rate in high shear regime($10^{1}s^{-1}$ to $10^{2}s^{-1}$). (d) and (e) are zoom-ins of (c).

DI, 0.8 and 1.79 for 100% DI, and 0.57 and 1.58 for the 7.5% DI dispersions. For Region III, the scaling exponents were 2.06 for 50% DI, 1.51 for 7.5% DI, and 0.92 for 100% DI dispersions. Our exponent values for all regions are consistent with previous literature[42,45,46]. The slope changes, even at such high shear rates, serve as a good indicator of the different concentration-based transitions, however, the scaling exponents at high shear rates might differ considerably, which have been used previously to identify semi-dilute, entangled, and concentrated regimes[46].

In 100% DI (Figure 5a), Region I, corresponds to the dilute regime and is in good agreement with the results we reported in Section 3.2. The predicted overlap concentration (c*) i.e. the transition from dilute to semi-dilute regime, can be estimated from equation 3 where the theoretically determined crowding factor for the dilute regime is $N_{3D} = 1$.[41] Given the previously calculated aspect ratio of 358, the corresponding volume fraction for the transition is 1.17×10^{-5} or 0.0017 wt.%, considering the density of cellulose to be 1.5 g/cm^3. At this concentration, the pervaded volume of the CNFsis the same as the volume of the solution. Upon further increase in the CNF volume fraction, Region II is reached, where there is an increase in the mobility constraints, as reflected by the increase in viscosity. At higher concentrations, the dispersions transition into Region III, which marks the semi-dilute region with higher volumetric overlap as described by Benselfelt et al.[41]. Literature showed the complete dilute to semi-dilute transition comparable to the overlap concentration of classical soluble polymers as the limit where there is a Newtonian to viscoelastic transition[41,42], representing the 3D volumetric overlap of individual fibers with N_{3D}=16. Our oscillatory rheology data shown in 6a-c also corroborate the Newtonian to viscoelastic transition at a volume fraction of 1.17×10^{-4} or about 0.02 wt.%.

For our IPA-containing solvents, the slope changes in Figure 5b-c show that the beginning of the dilute to semi-dilute transition, where N_{3D}=1, is reached at higher volume fractions than in the colloids suspended in pure water. Thus, cellulose-solvent pairs with a lower χ parameter have higher overlap concentration. The dilute to semi-dilute transition shifts from 0.0017 wt.% (case of 100% DI) to concentrations in the range of 0.0073 wt.% and 0.012 wt.%, respectively for 50% DI and 7.5% DI. The N_{3D}=16 transition also appears to shift from the window of 0.05 wt.% − 0.013 wt.% to a window of 0.023 − 0.03 wt.% and 0.02 wt.% − 0.055 wt.% for 50% DI and,7.5% DI, respectively. Such shifts in concentration-based regime transitions are a clear indication of the effect of thermodynamic interaction parameters on the colloidal behavior of nanocellulose. It is also important to understand that equation 3, fails to predict the concentration-based transitions when the thermodynamic interaction parameter is changed. While this relationship has been widely used for cellulose-water dispersions, its validity is limited upon changing the solvent (and thus χ interaction parameter), as in such cases transitions shift to higher volume fractions. One of the primary reasons for this would be that this relationship is more appropriate for stiff rod-like structures such as CNCs and not long semi-flexible CNF fibers. Further, it doesn't take into account the interaction parameters that are instrumental in polymer physics on the scaling of overlap concentrations.

Experimentally, we can observe the transitions between the di-

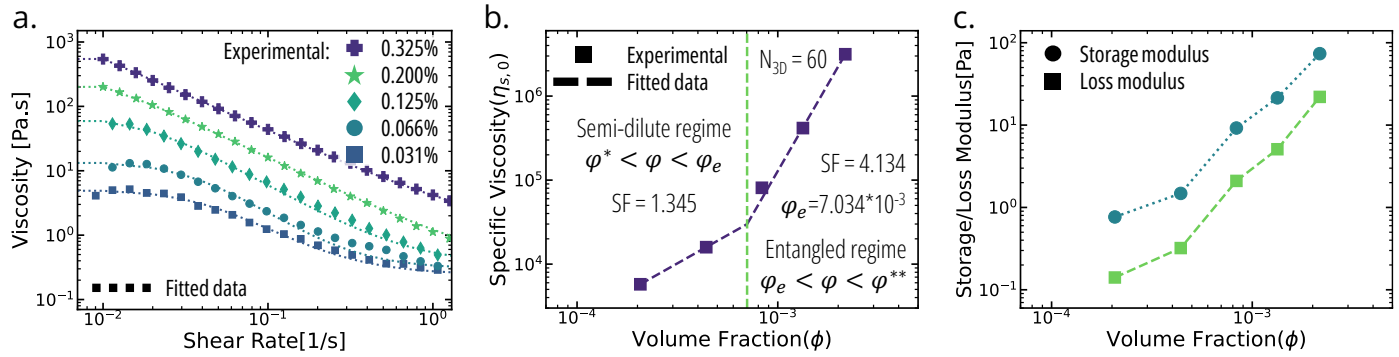

Fig. 4 Rheological Characterization of CNF. (a) Carreau model fit of viscosity data of CNF dispersions from 0.031 to 0.325 wt.%. (b) Specific viscosity against volume fraction depicting the transition from semi-dilute to entangled regimes. (c) Loss and storage modulus versus volume fraction.

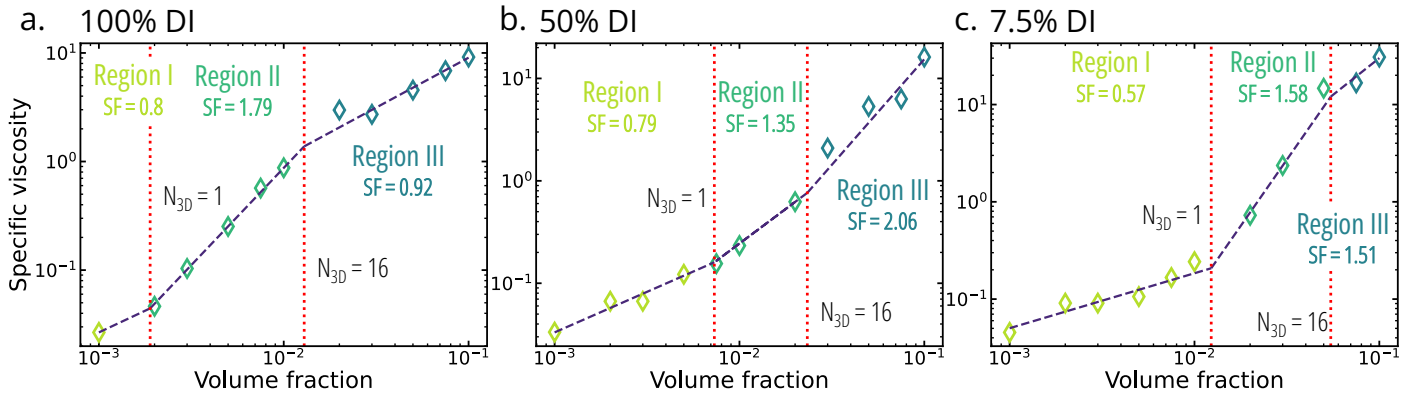

Fig. 5 Concentration-based regime transitions. Specific viscosity versus volume fraction for (a) 100% DI, (b) 50% DI and (c) 7.5% DI suspensions.

lute and semi-dilute regimes as the limits between Newtonian to viscoelastic behaviors through oscillatory rheological measurements, as previously stated. In Figure 6a-c the loss and storage moduli are plotted across all solvents for all CNF concentrations. The crossover point between storage and loss modulus, representing the Newtonian to Viscoelastic transition, is expected at the concentration corresponding to crowding factor N_{3D}=16. From our experimental results, we observe a transition window marked by the slope change and the crossover point, rather than a discrete point (where the crossover point and the slope change concentration would overlap into a single concentration point value). In our measured data this transition window is highlighted as a red-filled area in Figure 6. This can be attributed to the high polydispersity of cellulose nanofibers obtained from bacterial cultures[50].

The relative viscosities generally increase with the increase in thermodynamic interaction parameter (χ) as seen in 6d and SI Figure S4 at very low CNF volume fractions within the dilute regime, showing the following trend: $\eta_3 > \eta_2 > \eta_1$ where, $\chi_1 > \chi_2 > \chi_3$ (index 1 standing for 100% DI, index 2 for 50% DI, and index 3 for 7.5% DI). In the dilute regime, the CNFs are widely separated and have no hydrodynamic interactions. For a solvent with a lower χ parameter, the solvent molecules interact and penetrate the CNF clusters more, resulting in an increased excluded volume, which then causes an increase in relative viscosity. On increasing the χ interaction parameter, the polymer-polymer interaction forces increase and cause a reduction in the excluded volume, which is marked by a reduction in relative viscosity. In the semi-dilute region ($1 < N_{3D} < 16$), the volume fraction of CNF increases and starts hydrodynamically interacting and competing for space with one another. The excluded volume is therefore reduced by the increase of the volume fraction of CNFs. As the CNF volume fraction increases, the fibers are crammed together and overlap, which increases the intermolecular forces, especially the polymer-polymer interaction forces which significantly increase viscosity. Thus, in thermodynamically inferior solvents, there is an increased viscosity compared to solvents with a lower χ parameter. Indeed, our data (Figure 6d and SI Figure S4) show that for the case of 100% DI-suspended CNFs, there is a rapid increase in the viscosity compared to the other two solvents, primarily because these dispersions start transitioning from a dilute to a semi-dilute regime much before the IPA-containing dispersions. Further, at concentrations from 0.01 to 0.03 wt.% when all three dispersions are beyond the collision threshold ($N_{3D} = 1$), we see $\eta_1 > \eta_2 > \eta_3$. Such behavior conforms well to the established understanding of polymer rheology at dilute and semi-dilute regimes.[51].

Interestingly, we observe a deviation from the ideal trend of $\eta_1 > \eta_2 > \eta_3$, based on the trend in interaction parameter($\chi_1 > \chi_2 > \chi_3$) above the concentration of 0.03 wt.%. At concentrations higher than that threshold, the fiber-fiber interactions be-

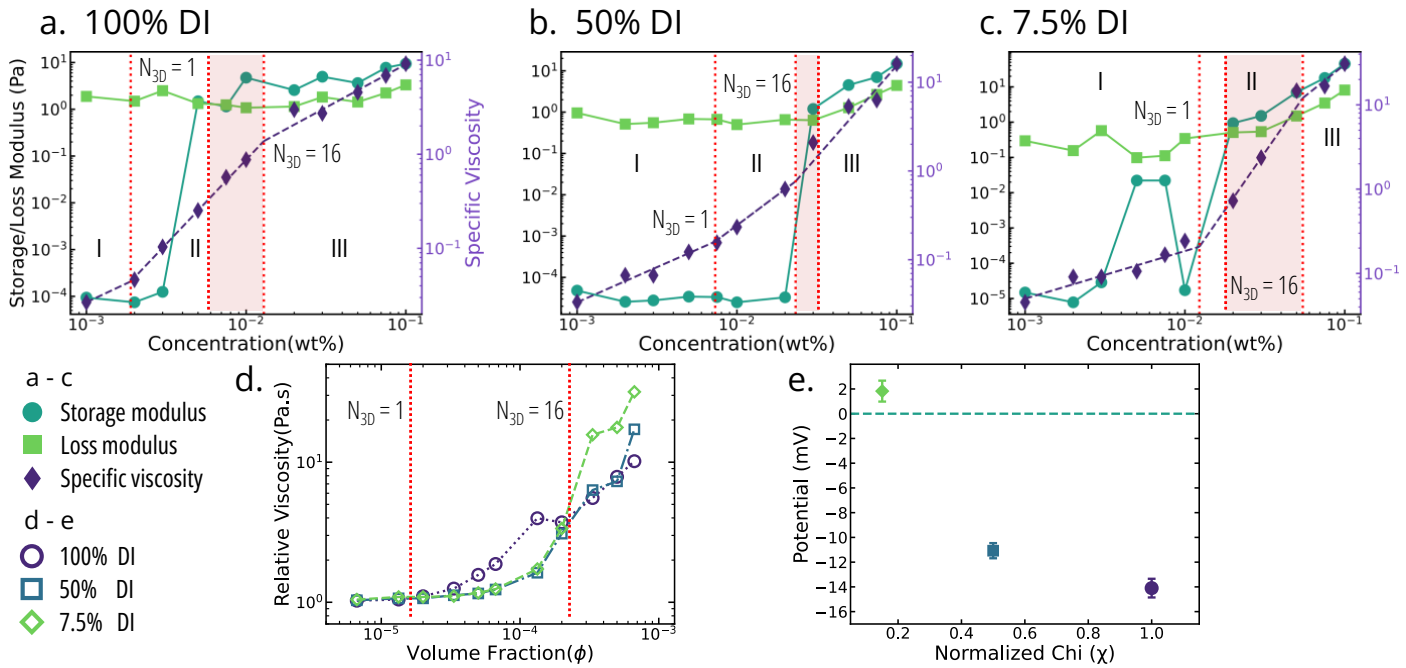

Fig. 6 Rheological study of thermodynamic behavior. Specific Viscosity, loss and storage modulus scaling with concentration, depicting the concentration-based transition for (a) 100% DI, (b) 50% DI, and (c) 7.5% DI suspensions. (d) Plot comparing relative viscosity against concentration for the three dispersions, with the region below $N_{3D} = 1$ line representing all the dispersions being in a dilute regime and the region beyond $N_{3D} = 16$ representing all the dispersions being in the semi dilute regime. (e) Electrokinetic stabilization of CNF in the three solvents. *The Y axes of (a) also apply to (b) and (c).

come significant, and thus interactive Van der Waals forces play an important role unless stabilized by electrostatic repulsion. In these conditions, the colloids enter the semi-dilute region, such that $N_{3D} > 16$ in 100% DI dispersions, while being in the $N_{3D} = 16$ window for concentrations of 50% and 7.5% DI. This deviation can be explained by the presence of lower electrokinetic stabilization in IPA-containing solvents (50% DI and 7.5% DI) compared to 100% DI. Corroborating this observation, Figure 6e shows the zeta potential of CNF in the 3 different solvents at their natural pH (without the addition of any acid or base). The CNF suspension in the 7.5% DI has a zeta Potential of 1.82 ± 0.85 mV, while the 50% DI sample has -11.1 ± 0.61 mV and the 100% DI-suspended CNFs have the lowest zeta potential of -14.1 ± 0.75 mV. Thus, the absolute lowest zeta potential of the 7.5% DI sample results in stronger Van der Waals attraction in the hydro clusters formed while the 50% DI and 100% DI samples experience electrostatic stabilization effects.

Figure 7, shows the solvent subtracted merged ESAXS and SAXS profiles for 0.001 wt.% CNF dispersion in the 3 different solvents and the Bayesian Indirect Fourier Transform (BIFT) Fitting. Guinier Fitting (SI for the fitting information and Residual Plots) in the low q region($qR_g < \pi$) yields the RMS radius of gyration of the CNF fibers in the three different solvents. For 100% DI, the R_g was estimated to be 30.5 nm, for the 7.5% DI it was 41 nm and for 50% DI it was 37 nm. The trend in R_g value with χ parameter reflects upon how the excluded volume increases with the decrease in the χ parameter due to the CNF unfolding or debundling. It must be noted that any form of agglomeration would also increase the R_g value. For confirming the R_g value of CNF in the dispersions, the pair distance distribution function was plotted against radius ($P_{(r)}$ versus r) and normalized Kratky Plots of the three dispersions were compared. The extended tail in the pair distribution plot (Figure 7b) in the 7.5% DI and 50% DI solvents when compared to 100% DI, can be attributed to the CNF unfolding/chain extending. The peak in the same plot corresponds to the R_g predictions from the BIFT fitting, which is in agreement with the Guinier Fit (despite Rg.q >1.3 in all three solvents for the Guinier Plots). The Normalized Kratky Plots for the three solvents (Figure 7c), show a characteristic for cellulose extended tail after a peak[52] reaching a plateau value. In pure water, we see a steeper downward slope before reaching the plateau value when compared to the other two solvents. In general, a steeper slope corresponds to a higher degree of fiber coiling and a flatter slope signifies fiber unfolding. Thus, from the R_g values, the distance distribution plot, and Kratky plots collectively, the CNF-solvent thermodynamic interaction and nanofiber morphology can be established, where IPA-containing solvents appear to be thermodynamically superior to water, which validates the rheological behavior observed before. We note that SAXS was collected for 0.001 wt.% which falls in the dilute regime in all three solvents. At such low concentrations, the inter-fiberentanglements and interactions become less significant and the conformation of individual nanofibers contributes to higher relative viscosities in the rheological properties of the dispersions as there is minimal hydrodynamic interaction between the fibers due to the absence of fiber entanglements. An increase in the excluded volume, arising

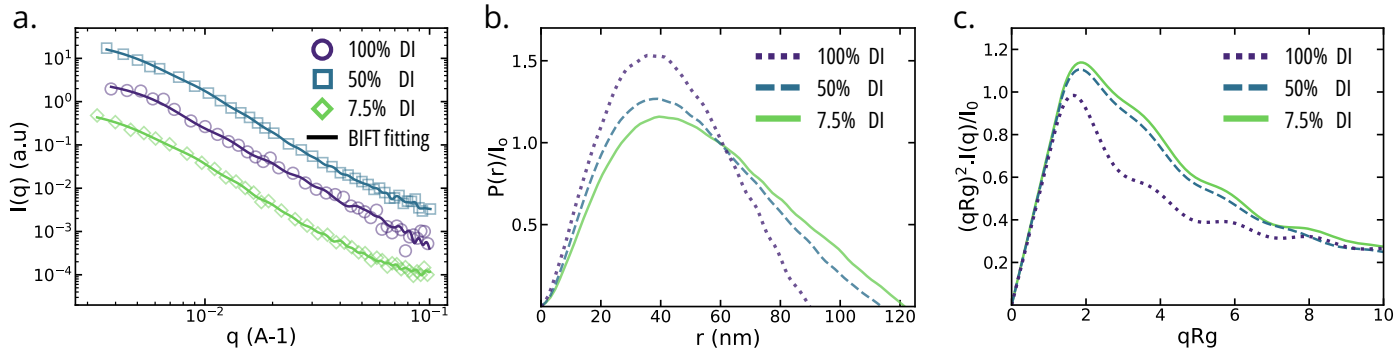

Fig. 7 X-ray Scattering of CNF Dispersions. (a) Experimental Data and BIFT Fitting. (b) Pair distance distribution plot. (c) Kratky Plot.

from a more open or extended conformation owing to a solvent-induced swelling results in a greater radius of gyration.

We emphasize that in CNF systems, unlike traditional synthetic polymers, deviations in C^* and R_g relationship can be seen compared to classic soluble polymers where $C^* \propto \frac{1}{R_g{}^3}$. In the CNF case, it is observed that despite the R_g of CNFs increasing in IPA-containing solvents due to chain unfolding, the dilute to semi-dilute regime transition C^* is shifted to higher CNF concentrations. Such deviations stem from the fact that these relationships are derived for polymers that are soluble in a chosen solvent, which does not apply to CNFs in our chosen solvents. Rather than being dissolved, the CNFs are dispersed as colloids in our suspensions.

Thus, to aptly understand the CNF behavior, both DLVO (electrostatic) and Flory-Huggins (thermodynamic) theory need to be taken into account for understanding the dilute to semi-dilute transition, as the fiber-fiber interactions in the semi-dilute transitions are greatly affected by the polymer as well as colloidal behavior. Individual cellulose chains are held together by secondary bonding (hydrogen and Van der Waals bonding) in highly crystalline large-aspect ratio fibrillar arrangements. These individual fibrils, in turn, twist with each other and are held by long-range interactions at a right-handed chirality forming nanofibers, which are dispersed as colloids in our solvent. The radius of gyration, in our case, is not representative of the individual cellulose chain but rather reflects the distribution of the nanofibers into a microfibrillar arrangement. Thus, a larger radius of gyration denotes a higher excluded volume as the nanofibers swell and extend, while a smaller radius of gyration suggests nanofibers tightly packed into microfibers with lower excluded volume.

From the rheological, zeta potential, and x-ray scattering measurements, it can be concluded that thermodynamic interactions play an important role in the colloidal behavior of CNFs, however, it is important to understand that the thermodynamic, electrokinetic, and hydrodynamic interactions act in tandem with one another towards nanocellulose colloidal behavior.

3.4 Effect of Thermodynamic Parameter on Microstructural and Mechanical Properties of Films

We prepared films from all the 0.2 wt.% dispersions and studied their tensile behavior as well as the morphology of the fracture surfaces. The tensile tests (Figure 8) showed a typical CNF film stress-strain behavior with a characteristic elastic region at low strains that is followed by a yielding and finally, a linear region of stain-hardened plastic deformation before the failure at low strains (stress-strain curves of individual samples provided in SI Figure S8). The films obtained from CNFs suspended in the 50% DI solvent showed superior strength, modulus and toughness, followed by the pure water suspended CNFs, with the 7.5% DI-suspended CNFs showing inferior performance across the board.

Specifically, the CNF samples suspended in 50% DI showed Young's modulus of 7.61 ± 1.12 GPa, which is 43% higher than the water-suspended sample (5.3 ± 0.56 GPa) and 520 % higher than the 7.5% DI-suspended sample (1.22 ± 0.09 GPa). The tensile strength of the 50% DI solvent sample (100.55 ± 10.83 MPa) was 23% and 540% higher than that of the water-suspended sample (81.57 ± 7.37 MPa) and 7.5% DI-suspended sample (15.67 ± 1.02 MPa), respectively. The toughness of the 50% DI sample and water-suspended sample were comparable, 1.88 ± 0.19 MJ/m^3 and 1.79 ± 0.27 MJ/m^3 respectively, whereas the 7.5% DI samples were considerably lower at 0.37 ± 0.05 MJ/m^3.

To understand the trends in the mechanical properties better, we further analyzed the sample morphologies in SEM, by studying top surfaces of the undeformed samples and fractured surfaces of the CNF films. For films obtained from the 50% DI and 100% DI solvents (Figure 9)a-f, the top surface SEM images showed the fibers to be much more tightly packed than 7.5% DI, which makes the later films much more porous owing to the increased excluded volume in the colloidal state, thus resulting in a film with inferior mechanical properties, corroborating the results reported in Figure8. Moreover, image analysis of the fracture cross-sections shown in SI Figures S7-S11, provided an estimate of the surface roughness, revealing roughness increases in the film fracture surface obtained from 50% DI to 100% DI to 7.5% DI. The same analysis provides a void count, which follows a trend of 7.5% DI > 100% DI > 50% DI. The analysis also quantified the average area fraction of voids and fiber pull-out which were estimated to decrease from the 50% DI to the 100% DI samples to the 7.5% DI. Higher fracture surface roughness has been generally associated with higher toughness[53], as a rough cross-section surface may indicate extensive plastic deformation before failure. Therefore the observation that CNFs in 7.5% DI have the

Solvent	Normalized χ (χ/χ_w)	Zeta Potential(mV)
100% water	1	-14.1 $\pm$ 0.75
7.5% water/92.5% IPA	0.15	1.82 $\pm$ 0.85
50% water/50% IPA	0.5	-11.1 $\pm$ 0.61

Table 2 Table summarizing the Zeta Potential(in mV) for CNF dispersions in different solvents(Normalized χ)

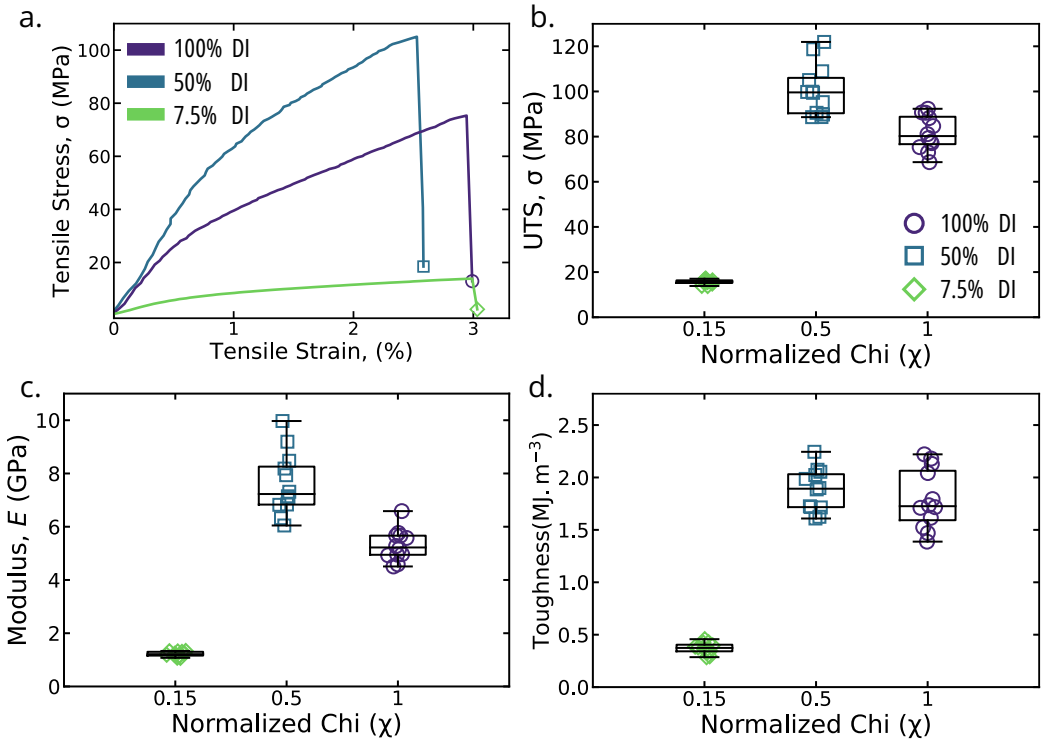

Fig. 8 Mechanical Properties of CNF Films. (a) Characteristic stress-strain curves for the CNF films.(b) ultimate tensile strength,(c) Young's modulus, and (d) toughness of the CNF films from the different solvents.

(For all tests, n=12)

lowest roughness correlates well with our mechanical testing results. A higher count of voids on the fracture surface, on the other hand, often can act as a double-edged sword when no mechanical testing data are available. While higher energy absorption is suggested by increased counts of fiber pull-outs, contributing to tougher performance, voids act as stress concentrators initiating crack propagation and causing inferior mechanical properties.

Overall, the SEM images of the fracture surfaces of CNFs from pure water (Figure 9a-c) or 50% DI (Figure 9d-f) dispersions reveal the characteristic layered structure of CNF films, as well as the interlayer fiber bridging and fiber pull-out upon failure, in agreement to prior literature[54–56]. Both those samples show significantly more fibrillation and fiber pull-out than the 7.5% DI sample, which supports their significantly higher toughness. We note a slightly higher inter-layer distance in the pure water sample compared to the 50% DI, which corroborates the slightly higher strength and toughness of the latter sample, albeit their difference was small. The most striking differences in morphology can be seen from the cross-section views of the 7.5% DI sample (Figure 9g-h), which reveals that it lacks the characteristic layered structure that the other two samples have. This in addition to the clearly higher porosity of the 7.5% DI sample, which can be attributed to the increased excluded volume of the fibers and swelling of gels in IPA, corroborates the mechanically inferior performance. Thus, the morphology of the samples confirms that the deformation behavior and failure of the CNF films are directly influenced by the solvent composition used during their preparation. Taken together, our results show that the higher IPA amounts in the colloidal state, which allow higher cellulose-solvent interactions and lead to a near-zero zeta potential at concentrations above the semi-dilute regime threshold, cannot prevent significant agglomeration which ultimately leads to the formation of CNFs with limited mobility which prevents the formation of a layered CNF structure, thus leading to inferior strength and toughness. On the other hand, with water concentration increasing in the colloidal state, even though cellulose-solvent interactions are more limited and fiber bundles with overall higher zeta potential are formed, above the semi-dilute regime threshold the bundle electrostatic repulsions may prevent larger aggregates from forming, allowing them the mobility needed to assemble into layers which is critical to ensure high strength and toughness. The 50% DI sample which showed the most superior me-

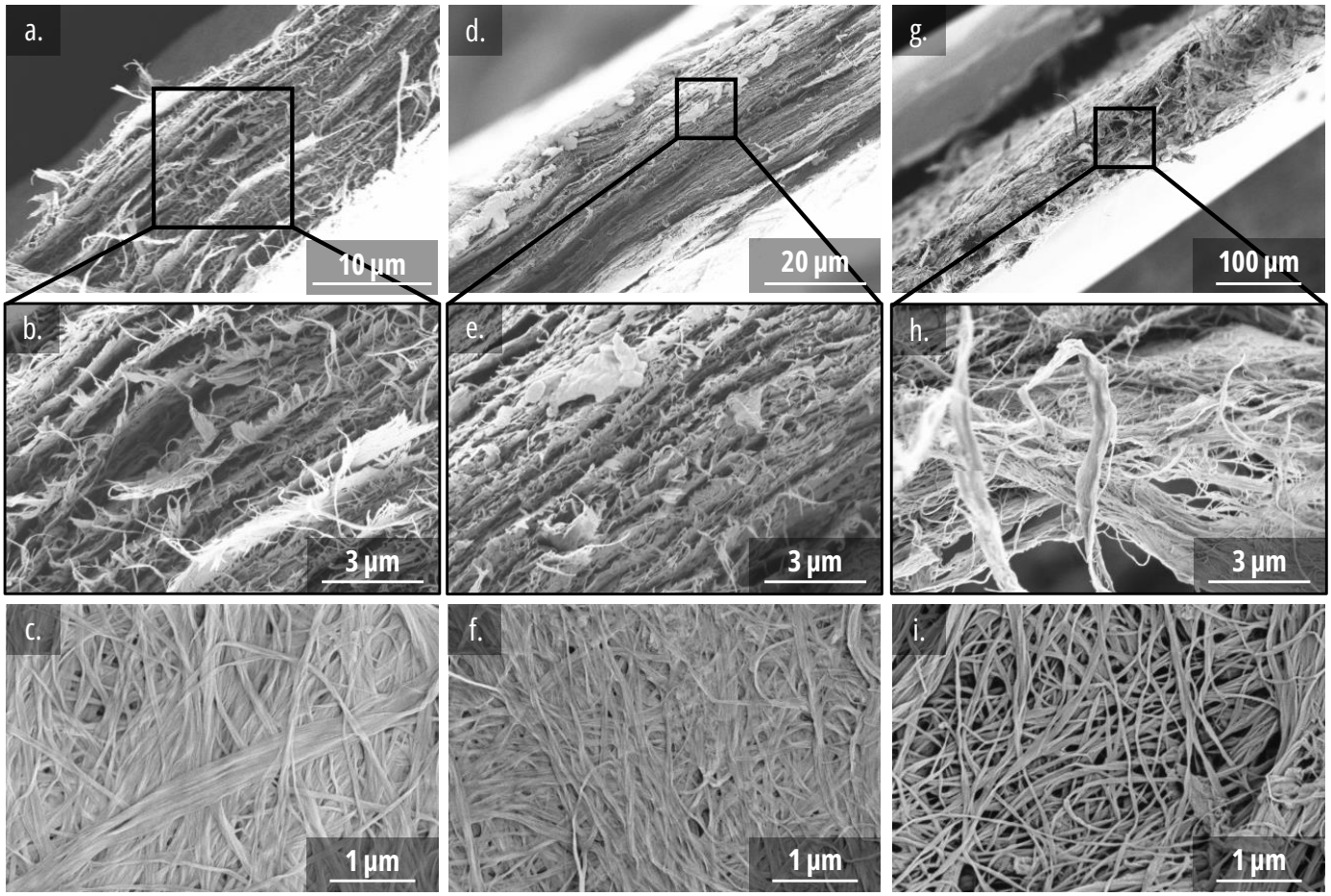

Fig. 9 SEM microstructural observations of CNF Films. (a-b) Fracture surface and (c) top surface of non-tested films prepared from 100% DI dispersions. (d-e) Fracture Surface and (f) top surface of non-tested films prepared from 50% DI dispersions. (g-h) Fracture Surface and (i) top surface of non-tested films prepared from 7.5% DI dispersions.

chanical properties, has a zeta potential comparable to that of the 100% DI sample and thermodynamic interactions comparable to that of the 7.5% DI sample. This presents an optimum balance where thermodynamic and electrokinetic interactions are synergistic. This balance ensures that the fibers in the dispersion are both well-dispersed (due to electrostatic stability) and in a solvent environment that promotes strong interactions (thermodynamic compatibility) leading to microstructural assembly that contributes to higher mechanical properties.

4 Conclusions

Our study sheds light on the pivotal role of thermodynamic interactions in the dispersion of bacterial CNFs demonstrating the correlation between the colloidal properties and their profound impact on the mechanical properties of resultant films. By varying the Hansen solubility parameter, we have showcased the tunability of CNF-solvent interactions, leading to enhanced dispersion quality in the dilute regime. The adjusted CNF-solvent interactions were found to influence the transition thresholds between dilute and semi-dilute regimes. Our rheological tests revealed the occurrence of transition ranges instead of a single concentration separating the two regimes, which we attribute to the polydispersity of CNFs. Lower chi parameters which lead to chain unfolding, were found to push the regime transition windows to higher concentrations, which was corroborated by SAXS data showing an extended tail and increased radius of gyration indicating a larger excluded volume in low chi solvents. However, the electrokinetic effects are also key, as the solvents with higher chi parameters lead to higher overall changes in dispersions which ultimately influence fiber aggregation at the supra-fiber level. At higher concentrations, the impact of zeta potential effects becomes predominant, leading to agglomeration, particularly in low chi solvents.

Casting films from dispersions above the semi-dilute regime threshold demonstrated the importance of balancing the thermodynamic and electrokinetic forces during colloidal processing. CNF films cast from suspensions in lower chi parameter solvents showed restricted fiber mobility and higher fiber swelling which prevented the formation of a layered structure upon drying and resulted in more porous films. The lack of a layered structure and higher porosity result in lower strength, modulus, and toughness of those films as compared to films cast from CNFs suspended in higher chi parameter solvents. This outcome is closely linked to the dominant electrokinetic effects and low zeta potential of the CNFs in low chi solvents, explaining the observed differences

Tensile Properties	100 % v/v Water	7.5 % v/v Water in IPA	50 % v/v Water in IPA
UTS (MPa)	81.57±7.37	15.67±1.02	100.55±10.83
Young's Modulus (GPa)	5.4±0.56	1.22±0.09	7.61±1.12
Toughness (MJ/m^3)	1.79±0.27	0.37±0.05	1.88±0.19
Elongation Break (%)	3.58±0.33	3.52±0.35	2.97±0.31

Table 3 Tensile Properties of CNF Films. Table summarizing ultimate tensile strength (UTS), Young's Modulus, Toughness, and elongation break of the films prepared from CNF dispersions in 100% DI, 50% DI and 7.5% DI solvents.

in mechanical behavior. Moreover, the comparison between the two higher chi solvents, the 50/50 mixture of water/IPA and pure water, indicates that the former achieves a higher modulus and strength, attributable to the experimentally observed reduced interlayer distances. Our studies concluded that the balance between electrokinetic and thermodynamic interactions in CNF colloidal dispersion is essential for the fabrication of CNF bulk structures. Colloids with superior and more synergistic thermodynamic and electrokinetic interaction would lead to films with higher mechanical properties.

Author Contributions

Conceptualization, E.R.; Methodology, E.R., and A.M.; Formal Analysis, A.M. and K.L.; Investigation, A.M., K.L., H.I., X.L., J.L., and S.Z.; Resources, E.R.; Writing - Original Draft, A.M., E.R.; Writing - Review & Editing, A.M, H.I., K.L., X.L., S.Z., and E.R.

Conflicts of interest

There are no conflicts to declare.

Acknowledgements

This work was supported by the National Science Foundation, Division of Materials Research Award 2332640. The authors acknowledge the use of facilities and instrumentation supported by the U.S. National Science Foundation through the Major Research Instrumentation (MRI) program (DMR-2116265) and the UW Molecular Engineering Materials Center (MEM-C), a Materials Research Science and Engineering Center (DMR-2308979). The authors acknowledge Scott Braswell for assistance with Scanning Electron Microscopy, Abdul Mooez for SAXS beamline support, William Kuykendall for mechanical testing support, and Dr. Benjamin Rutz for rheometer assistance. Part of this work was conducted at the Molecular Analysis Facility, a National Nanotechnology Coordinated Infrastructure (NNCI) site at the University of Washington, which is supported in part by funds from the National Science Foundation (awards NNCI-2025489, NNCI-1542101), the Molecular Engineering & Sciences Institute, and the Clean Energy Institute. Part of this work was conducted at the Washington Clean Energy Testbeds, a facility operated by the University of Washington Clean Energy Institute.

Notes and references

1 D. Klemm, B. Heublein, H.-P. Fink and A. Bohn, *Angewandte Chemie International Edition*, 2005, **44**, 3358–3393.

2 D. Klemm, F. Kramer, S. Moritz, T. Lindström, M. Ankerfors, D. Gray and A. Dorris, *Angewandte Chemie International Edition*, 2011, **50**, 5438–5466.

3 D. Klemm, D. Schumann, F. Kramer, N. Heßler, M. Hornung, H.-P. Schmauder and S. Marsch, in *Nanocelluloses as Innovative Polymers in Research and Application*, Springer Berlin Heidelberg, Berlin, Heidelberg, 2006, pp. 49–96.

4 A. Hajian, S. B. Lindström, T. Pettersson, M. M. Hamedi and L. Wågberg, *Nano Letters*, 2017, **17**, 1439–1447.

5 A. E. Way, L. Hsu, K. Shanmuganathan, C. Weder and S. J. Rowan, *ACS Macro Letters*, 2012, **1**, 1001–1006.

6 D.-C. Wang, H.-Y. Yu, D. Qi, Y. Wu, L. Chen and Z. Li, *Journal of the American Chemical Society*, 2021, **143**, 11620–11630.

7 A. Ferguson, U. Khan, M. Walsh, K.-Y. Lee, A. Bismarck, M. S. P. Shaffer, J. N. Coleman and S. D. Bergin, *Biomacromolecules*, 2016, **17**, 1845–1853.

8 S. J. Eichhorn, A. Dufresne, M. Aranguren, N. E. Marcovich, J. R. Capadona, S. J. Rowan, C. Weder, W. Thielemans, M. Roman, S. Renneckar and et al., *Journal of Materials Science*, 2010, **45**, 1–33.

9 S. Gårdebjer, M. Andersson, J. Engström, P. Restorp, M. Persson and A. Larsson, *Polymer Chemistry*, 2016, **7**, 1756–1764.

10 J. Lang, N. Wang, X. Wang, Y. Wang, G. Chen and H. Zhang, *BioResources*, 2021, **16**, 7112–7121.

11 Y. Wang, Z. Yu, A. Dufresne, Z. Ye, N. Lin and J. Zhou, *ACS Nano*, 2021, **15**, 20148–20163.

12 C. Bruel, J. R. Tavares, P. J. Carreau and M.-C. Heuzey, *Carbohydrate Polymers*, 2019, **205**, 184–191.

13 R. J. Moon, A. Martini, J. Nairn, J. Simonsen and J. Youngblood, *Chem. Soc. Rev.*, 2011, **40**, 3941–3994.

14 B. L. Tardy, B. D. Mattos, C. G. Otoni, M. Beaumont, J. Majoinen, T. Kamarainen and O. J. Rojas, *Chemical reviews*, 2021, **121**, 14088–14188.

15 L. Wågberg, L. Winter, L. Ödberg and T. Lindström, *Colloids and Surfaces*, 1987, **27**, 163–173.

16 L. Wågberg, G. Decher, M. Norgren, T. Lindström, M. Ankerfors and K. Axnäs, *Langmuir*, 2008, **24**, 784–795.

17 S. N. Molnes, K. G. Paso, S. Strand and K. Syverud, *Cellulose*, 2017, **24**, 4479–4491.

18 B. A. Frost and E. Johan Foster, *Journal of Renewable Materials*, 2020, **8**, 187–203.

19 J. Araki, M. Wada, S. Kuga and T. Okano, *Colloids and Surfaces A: Physicochemical and Engineering Aspects*, 1998, **142**, 75–82.

20 Kusmono and M. N. Affan, *Journal of Natural Fibers*, 2020, **19**, 2744–2755.

21 S. Camarero Espinosa, T. Kuhnt, E. J. Foster and C. Weder, *Biomacromolecules*, 2013, **14**, 1223–1230.

22 T. I. Shaheen and H. E. Emam, *International Journal of Biological Macromolecules*, 2018, **107**, 1599–1606.

23 I. A. Sacui, R. C. Nieuwendaal, D. J. Burnett, S. J. Stranick, M. Jorfi, C. Weder, E. J. Foster, R. T. Olsson and J. W. Gilman, *ACS Applied Materials & Interfaces*, 2014, **6**, 6127–6138.

24 N. Pandi, S. H. Sonawane and K. Anand Kishore, *Ultrasonics Sonochemistry*, 2021, **70**, 105353.

25 Z. Shang, X. An, F. T. Seta, M. Ma, M. Shen, L. Dai, H. Liu and Y. Ni, *Carbohydrate Polymers*, 2019, **222**, 115037.

26 T. Cao and M. Elimelech, *Journal of Colloid and Interface Science*, 2021, **584**, 456–463.

27 W. Chen, H. Yu, Y. Liu, P. Chen, M. Zhang and Y. Hai, *Carbohydrate Polymers*, 2011, **83**, 1804–1811.

28 B. Derjaguin and L. Landau, *Progress in Surface Science*, 1993, **43**, 30–59.

29 B. V. Derjaguin, N. V. Churaev and V. M. Muller, *Surface Forces*, 1987, 293–310.

30 K. Wilson and J. M. Walker, *Principles and techniques of Biochemistry and Molecular Biology*, Cambridge University Press, 2007.

31 Y. Qing, R. Sabo, J. Zhu, U. Agarwal, Z. Cai and Y. Wu, *Carbohydrate Polymers*, 2013, **97**, 226–234.

32 A. B. Fall, S. B. Lindström, O. Sundman, L. Ödberg and L. Wågberg, *Langmuir*, 2011, **27**, 11332–11338.

33 J. N. Israelachvili, *Intermolecular and surface forces*, Academic Press,an imprint of Elsevier, 2012.

34 G. N. Balistreri, I. R. Campbell, X. Li, J. Amorim, S. Zhang, E. Nance and E. Roumeli, *RSC Applied Polymers*, 2024.

35 J. B. Hopkins, *Journal of Applied Crystallography*, 2024, **57**, 194–208.

36 P. A. Penttilä, T. Imai, M. Capron, M. Mizuno, Y. Amano, R. Schweins and J. Sugiyama, *Cellulose*, 2018, **25**, 2771–2783.

37 N. E.-A. El-Naggar, A. B. A. Mohammed and S. E. El-Malkey, *Scientific Reports*, 2023, **13**, 51.

38 W. Qi, J. Yu, Z. Zhang and H.-N. Xu, *Materials Research Express*, 2019, **6**,.

39 H. T. Winter, C. Cerclier, N. Delorme, H. Bizot, B. Quemener and B. Cathala, *Biomacromolecules*, 2010, **11**, 3144–3151.

40 E. J. Foster, R. J. Moon, U. P. Agarwal, M. J. Bortner, J. Bras, S. Camarero-Espinosa, K. J. Chan, M. J. D. Clift, E. D. Cranston, S. J. Eichhorn, D. M. Fox, W. Y. Hamad, L. Heux, B. Jean, M. Korey, W. Nieh, K. J. Ong, M. S. Reid, S. Renneckar, R. Roberts, J. A. Shatkin, J. Simonsen, K. Stinson-Bagby, N. Wanasekara and J. Youngblood, *Chem. Soc. Rev.*, 2018, **47**, 2609–2679.

41 T. Benselfelt, N. Kummer, M. Nordenström, A. B. Fall, G. Nyström and L. Wågberg, *ChemSusChem*, **n/a**, e202201955.

42 L. Geng, N. Mittal, C. Zhan, F. Ansari, P. R. Sharma, X. Peng, B. S. Hsiao and L. D. Söderberg, *Macromolecules*, 2018, **51**, 1498–1506.

43 J. Liao, K. A. Pham and V. Breedveld, *Cellulose*, 2020, **27**, 3741–3757.

44 A. Celzard, V. Fierro and R. Kerekes, *Cellulose*, 2009, **16**, 983–987.

45 J. Choi, K. S. Cho and M. K. Kwon, *Polymers*, 2022, **14**,.

46 E. Lasseuguette, D. Roux and Y. Nishiyama, *Cellulose*, 2008, **15**, 425–433.

47 F. Fneich, J. Ville, B. Seantier and T. Aubry, *Carbohydrate Polymers*, 2019, **211**, 315–321.

48 H. Kropholler and W. Sampson, *Journal of Pulp and Paper Science*, 2001, **27**, year.

49 J.-G. Park, S.-H. Lee, J.-S. Ryu, Y.-K. Hong, T.-G. Kim and A. A. Busnaina, *Journal of The Electrochemical Society*, 2006, **153**, G811.

50 H. Wang, L. Kong and G. R. Ziegler, *Food Hydrocolloids*, 2019, **90**, 90–98.

51 T. Strivens, *Paint and Surface Coatings (Second Edition)*, Woodhead Publishing, Second Edition edn, 1999, pp. 550–574.

52 H. Peng, X. Ning, S. Wang and A. Ju, *Cellulose*, 2018, **25**, 5499–5510.

53 A. J. Benítez, J. Torres-Rendon, M. Poutanen and A. Walther, *Biomacromolecules*, 2013, **14**, 4497–4506.

54 M. Zhao, F. Ansari, M. Takeuchi, M. Shimizu, T. Saito, L. A.Berglund and A. Isogai, *Nanoscale Horizons*, 2018, **3**, 28–34.

55 C. Cai, Z. Wei, Y. Huang, P. Wang, J. Song, L. Deng and Y. Fu, *Cellulose*, 2020, **27**, 10241–10257.

56 I. Hasan, J. Wang and M. Tajvidi, *Cellulose*, 2021, **28**, 11345–11366.